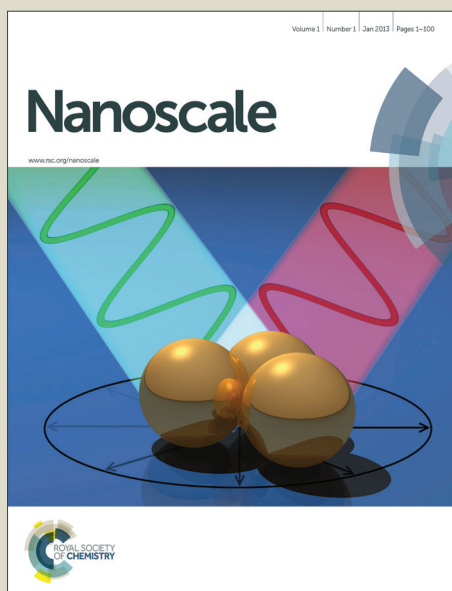


# Nanoscale

Accepted Manuscript



This is an *Accepted Manuscript*, which has been through the Royal Society of Chemistry peer review process and has been accepted for publication.

*Accepted Manuscripts* are published online shortly after acceptance, before technical editing, formatting and proof reading. Using this free service, authors can make their results available to the community, in citable form, before we publish the edited article. We will replace this *Accepted Manuscript* with the edited and formatted *Advance Article* as soon as it is available.

You can find more information about *Accepted Manuscripts* in the [Information for Authors](#).

Please note that technical editing may introduce minor changes to the text and/or graphics, which may alter content. The journal's standard [Terms & Conditions](#) and the [Ethical guidelines](#) still apply. In no event shall the Royal Society of Chemistry be held responsible for any errors or omissions in this *Accepted Manuscript* or any consequences arising from the use of any information it contains.

Cite this: DOI: 10.1039/c0xx00000x

www.rsc.org/xxxxxx

## ARTICLE

**“Smart” Theranostic Lanthanide Nanoprobes with Simultaneous Upconversion fluorescence and Tunable T<sub>1</sub>-T<sub>2</sub> Magnetic Resonance Imaging Contrast and Near-Infrared Activated Photodynamic Therapy**Yan Zhang,<sup>a</sup> Gautom Kumar Das,<sup>a</sup> Vimalan Vijayaragavan,<sup>b</sup> Qing Chi Xu,<sup>a</sup> Parasuraman Padmanabhan,<sup>c</sup> Kishore K. Bhakoo,<sup>b</sup> and Subramanian Tamil Selvan,<sup>d</sup> Timothy Thatt Yang Tan<sup>a\*</sup>

Received (in XXX, XXX) Xth XXXXXXXXX 20XX, Accepted Xth XXXXXXXXX 20XX

DOI: 10.1039/b000000x

The current work reports a type of “smart” lanthanide-based theranostic NaDyF<sub>4</sub>:Yb<sup>3+</sup>/NaGdF<sub>4</sub>:Yb<sup>3+</sup>,Er<sup>3+</sup> nanoprobes, which are able to circumvent the up-converting poisoning effect of Dy<sup>3+</sup> ions to give efficient near infrared (980 nm) triggered up-conversion fluorescence, and offers not only excellent dark T<sub>2</sub>-weighted MR contrast but also tunable bright and dark T<sub>1</sub> MR contrasts properties. Due to the efficient up-converted energy transfer from the nanocrystals to chlorin e6 (Ce6) photosensitizers loaded onto the nanocrystals, cytotoxic singlet oxygen was generated and photodynamic therapy was demonstrated. Therefore, the current multifunctional nanocrystals could be potentially useful in various image-guided diagnoses where bright or dark MRI contrast could be selectively tuned to optimize image quality, but also as an efficient and more penetrative near-infrared activated photodynamic therapy agent.

**1. Introduction**

Theranostic nanoprobes that combine imaging and therapy into a single matrix are highly desirable for image-guided diagnostic and treatment of cancer. Recent efforts that have been dedicated to construct such multifunctional platform include MnO<sub>2</sub>,<sup>1</sup> iron oxide,<sup>2-4</sup> gold,<sup>5-7</sup> and silica<sup>8</sup> etc. Lanthanide nanocrystals (NCs), in this regard, have been found suitable as theranostic agents due to their superior fluorescence and magnetism properties, which enable contrast enhancement in magnetic resonance imaging (MRI) with subsequent optical identification, and the ability to deliver therapeutic agents via systematic delivery.

In particular, they can convert near-infrared (NIR) photons (usually 980 nm) to higher energy photons ranging from UV to NIR, a process known as up-conversion (UC), with benefits include minimum photodamage, low autofluorescence, high signal-to-noise ratio and high penetration depth in biological

can act as a type of new-generation photosensitizers (PS) carriers, which can potentially overcome the drawbacks in current photodynamic therapy (PDT). Current PDT uses visible or even UV light as excitation source to activate PSs and generate cytotoxic reactive oxygen species (ROS) to induce cell death.<sup>10</sup> It suffers from limited penetration depth due to the light absorption and scattering by biological tissues, causing ineffective therapeutic effects. The UC emissions of the NCs, therefore, can activate the PSs attached on the NCs and produce ROS to kill cancer cells.

Moreover, paramagnetic gadolinium (Gd<sup>3+</sup>) or dysprosium (Dy<sup>3+</sup>) ions-containing NCs can effectively enhance MR imaging by decreasing the relaxation time of nearby water protons via process called spin-lattice relaxation (T<sub>1</sub>) or spin-spin relaxation (T<sub>2</sub>), respectively. Due to 4f<sup>7</sup> electronic configuration, Gd<sup>3+</sup>-based NCs are commonly used as T<sub>1</sub> bright MRI contrast agents (CAs). Dy<sup>3+</sup> ions, on the other hand, are commonly employed as T<sub>2</sub> CAs due to their higher magnetic moment (10.6 μ<sub>B</sub>) and shorter electronic relaxation time (~ 0.5 ps).<sup>11-13</sup> However, they are notorious as UC poison. Previous studies have attempted to utilize the T<sub>1</sub>/T<sub>2</sub> dual-mode MR imaging simultaneously, which can synergize the contrast effect in both T<sub>1</sub> imaging with high tissue resolution and T<sub>2</sub> imaging with high feasibility of detection of a lesion, leading to complementary data.<sup>14</sup> Reports are mainly focused on using magnetic iron oxide as T<sub>2</sub> CAs and Gd-chelates/NaGdF<sub>4</sub>/MnO as T<sub>1</sub> bright CAs.<sup>14,15-20</sup> As Dy-based NCs are particularly useful in high magnetic field, which provides advantages of higher signal-to-noise ratio, high speed and high resolution imaging, we wonder how to integrate two Gd<sup>3+</sup> and Dy<sup>3+</sup> ions within a single nanomatrix to achieve tunable T<sub>1</sub>-T<sub>2</sub> MRI contrast and strong UC emissions, and their subsequently

<sup>a</sup> School of Chemical and Biomedical Engineering, Nanyang Technological University, 62 Nanyang Drive, Singapore 637459. Fax: (+65) 6794 7553; Tel: (+65) 6592 1614; E-mail: [tytan@ntu.edu.sg](mailto:tytan@ntu.edu.sg)

<sup>b</sup> Translational Molecular Imaging Group, Singapore Bioimaging Consortium, Helios Building, 11 Biopolis Way, Singapore 138667.

<sup>c</sup> The Lee Kong Chian School of Medicine, Nanyang Technological University, 50 Nanyang Drive, Research Techno Plaza, Level 4, X-Frontier Block, Singapore 637553.

<sup>d</sup> Institute of Materials Research and Engineering, 3 Research Link, Singapore 117602.

† Electronic Supplementary Information (ESI) available: [details of any supplementary information available should be included here]. See DOI: 10.1039/b000000x/

tissues.<sup>9</sup> Besides being employed in bioimaging, lanthanides NCs

application in PDT, which has not yet been reported to our best of knowledge.

Herein, to circumvent the quenching of  $\text{Dy}^{3+}$ ,  $\text{NaDyF}_4:\text{Yb}^{3+}$  seed particles were first grown, which underwent further growth in the presence of  $\text{Gd}^{3+}$ ,  $\text{Yb}^{3+}$  and  $\text{Er}^{3+}$  ions to form nanorods (NRs) (i.e.  $\text{NaDyF}_4:\text{Yb}^{3+}/\text{NaGdF}_4:\text{Yb}^{3+},\text{Er}^{3+}$ ) (schematic is presented in Fig. 1a). Fluoride hosts have been chosen for their strong and efficient UC due to their high chemical stability and low photon energies ( $\sim 350 \text{ cm}^{-1}$ ).<sup>21, 22</sup> Ytterbium ( $\text{Yb}^{3+}$ ) sensitizer ions were chosen to be doped into both layers of the matrix as  $\text{Yb}^{3+}$  ions possess single excited state at 980 nm and higher absorption cross-section, rendering the UC or energy transfer process more efficient.<sup>23, 24</sup>  $\text{Gd}^{3+}$  ions were chosen in the outermost layer to facilitate direct contact with the bound water molecules to induce electron-nuclear dipolar interactions with the surrounding water protons, hence shortening the  $T_1$ , while  $\text{Dy}^{3+}$  ions in the core induce spin-spin interactions and produce  $T_2$  dark contrast. The resultant NCs show simultaneous tunable both negative and positive  $T_1$  contrast and  $T_2$  contrast enhancement in MRI *in vitro* and *in vivo* and strong UC fluorescence. Chlorin e6 (Ce6), a typical PS, was incorporated in the NCs and its near infrared (under 980 nm irradiation) triggered PDT effect was demonstrated.

## 2. Synthesis and Characterization

### 2.1 Materials:

Gadolinium (III) chloride hexahydrate (99.9%), ytterbium (III) chloride hexahydrate (99.9%), erbium (III) chloride hexahydrate (99.9%), dysprosium (III) chloride hexahydrate (99.9%), sodium hydroxide (99%), ammonia fluoride (99%), sodium oleate (90%), octadecene (90%), oleic acid (90%), poly(maleic anhydride-alt-1-octadecene) (PMAO), poly(ethylene glycol) methyl ether (PEG-OH), 9,10-dimethylanthracene (DMA) were purchased from Sigma-Aldrich and used without further purification. Sulfuric acid (98%0 was purchased from Merck. Chorin e6 was purchased from Frontier Scientific, Inc. Ethanol, hexane, chloroform and diethylether were purchased from Aik Moh.

### 2.2 Synthesis of $\text{NaDyF}_4:\text{Yb}^{3+}/\text{NaGdF}_4:\text{Yb}^{3+},\text{Er}^{3+}$ NCs

To synthesize  $\text{NaDyF}_4:\text{Yb}^{3+}/\text{NaGdF}_4:\text{Yb}^{3+},\text{Er}^{3+}$  NCs, lanthanide-oleate complexes ( $\text{Ln} = \text{Dy}, \text{Yb}, \text{Gd}, \text{Er}$ ) were synthesized based on a modified method.<sup>25</sup> The Dy-oleate and Yb-oleate complexes were then dissolved in oleic acid and 1-octadecene (15 ml / 15 ml) at room temperature. The mixture was heated to 150 °C for 30 min to form a clear solution under the protection of nitrogen gas. After cooling the solution to 60 °C, 10 ml methanol solution containing  $\text{NH}_4\text{F}$  (4 mmol) and  $\text{NaOH}$  (2.5 mmol) was added into the flask and the solution was maintained at 60 °C for 30 min. The resulting solution was heated to 300 °C and kept at that temperature for 2 h. The resulting solution was cooled to room temperature and the NCs were obtained after washing with ethanol and hexane three times. Finally, the  $\text{NaDyF}_4:\text{Yb}^{3+}$  NCs were dispersed in hexane.

$\text{Gd}(\text{oleate})_3 \cdot 6\text{H}_2\text{O}$  (0.8 mmol),  $\text{Yb}(\text{oleate})_3 \cdot 6\text{H}_2\text{O}$  (0.18 mmol),  $\text{Er}(\text{oleate})_3 \cdot 6\text{H}_2\text{O}$  (0.02 mmol), oleic acid (15 ml) and octadecene (15 ml) were mixed in a 100 ml three-necked reaction flask. The mixture was heated to 150 °C under the protection of nitrogen gas for 30 min to form a clear solution. Afterwards, the seed  $\text{NaDyF}_4:\text{Yb}^{3+}$  NCs in 10 ml hexane was added to the above solution and stirred for 30 min. After the removal of hexane, 10

ml methanol solution containing  $\text{NH}_4\text{F}$  (4 mmol) and  $\text{NaOH}$  (2.5 mmol) was added into the flask and the solution was maintained at 60 °C for 30 min. Then, the flask was heated to 300 °C, and kept at this temperature for 2 h under vigorous stirring to form the final NRs. After the reaction, the solution was cooled down to room temperature, and washed with ethanol and hexane for three times. The  $\text{NaDyF}_4:\text{Yb}^{3+}/\text{NaGdF}_4:\text{Yb}^{3+},\text{Er}^{3+}$  NRs were obtained after washing and they were readily dispersed in organic solvents such as hexane, cyclohexane, toluene and chloroform.

### 2.3 Synthesis of amphiphilic PMAO-PEG polymer.

PMAO-PEG was synthesized following Yu et al. protocol with modifications.<sup>26</sup> In a typical synthesis, 1g of PMAO and 1.5 g of PEG-OH were dissolved in 10 ml chloroform. 50  $\mu\text{l}$  of concentrated  $\text{H}_2\text{SO}_4$  was added to it. The mixture was refluxed at 60 °C overnight. The mixture was then neutralized using 1M  $\text{NaOH}$  followed by centrifugation to remove salt and water. The clear dispersion of PMAO-PEG (MW = 17832, polydispersity 1.7327) in chloroform was later added dropwisely into 250 ml diethylether to precipitate the polymer. The precipitated polymer was filtered, washed with ether, dried and subsequently lyophilized.

### 2.4 Surface modification of $\text{NaDyF}_4:\text{Yb}^{3+}/\text{NaGdF}_4:\text{Yb}^{3+},\text{Er}^{3+}$ .

PMAO-PEG (100 mg) was dissolved in 9 ml chloroform and the  $\text{NaDyF}_4:\text{Yb}^{3+}/\text{NaGdF}_4:\text{Yb}^{3+},\text{Er}^{3+}$  dispersion in chloroform (1 ml) was added to the solution and the solution was stirred overnight at room temperature. Then, chloroform was removed slowly using a rotary evaporator at room temperature, leaving a waxy layer in the flask. About 15 ml of distilled water was then added to the waxy liquid and dispersed well by sonication for 15 min. The flask was mounted back to the rotary evaporator and removed the remaining chloroform. The NCs were then collected using centrifuge and redispersed in 10 ml distilled water.

### 2.5 Loading Ce6 to PEG-functionalized $\text{NaDyF}_4:\text{Yb}^{3+}/\text{NaGdF}_4:\text{Yb}^{3+},\text{Er}^{3+}$ .

Ce6 was mixing with  $\text{NaDyF}_4:\text{Yb}^{3+}/\text{NaGdF}_4:\text{Yb}^{3+},\text{Er}^{3+}$  NCs in phosphate buffer solution (PBS) at room temperature for 24 h. Free Ce6 was removed by centrifugation at 10000 rpm for 10 min and washed 3 times with PBS buffer. The formed composite was redispersed in PBS.

### 2.6 Determination of generation of singlet oxygen.

20 mM of DMA stock solution was prepared. Samples containing NCs-Ce6 and DMA were irradiated using a 980 nm laser source (BWF-2,  $P_{\text{max}} = 2.0 \text{ W}$  at 3.0 A, B&W TEK Inc.). The decrease in fluorescence intensity of DMA ( $\lambda_{\text{ex}} = 360 \text{ nm}$  and  $\lambda_{\text{em}} = 380 - 550 \text{ nm}$ ) as a result of the generation of singlet oxygen was monitored using a Shimadzu RF-5301 PC spectrofluorometer fitted with a 150-W xenon lamp as the excitation source with a resolution of 1 nm. All samples were stirred before and during laser irradiation to ensure that light energy was dissipated by the entire volume of sample solution.

### 2.7 Cell viability assessment of PEG modified $\text{NaDyF}_4:\text{Yb}/\text{NaGdF}_4:\text{Yb},\text{Er}$

HeLa cells were maintained in Dulbecco's modified Eagle's medium (DMEM) supplemented with 10% fetal bovine serum (FBS), 100 U/mL penicillin and 100 I g/mL streptomycin, in a 5%  $\text{CO}_2$  environment at 37 °C with saturated humidity. The medium was changed every other day. Cells were subcultured upon 80 % confluency by 0.25 % trypsin-EDTA. To evaluate the

cytotoxicity of the NCs, HeLa cells were incubated with NCs as a function of NC concentration and incubation time. Data are presented as mean  $\pm$  standard deviation for three independent experiments. HeLa cells were plated in 96-well plates with a cell density of  $10^4$  cells per well and allowed to grow into full confluence. And then, the medium were replaced by refresh ones with NCs of different concentrations and the cells were incubated for 24 h, 48 h or 72 h, separately. Alamar blue assays (invitrogen) were performed at each time point. The cytotoxicity was expressed as the percentage of cell viability compared to that of untreated control cells.

## 2.8 Live/Dead Cell Viability Test

Cells were seeded into 24-well plates with a cell density of  $5 \times 10^4$  cells per well. After adhesion, the medium was replaced with or without serum-free medium containing NCs of different concentrations and the cells were incubated for 1 h. Then the medium was replaced with fresh serum-free medium and NIR laser irradiation was applied for 0, 10, 20 and 30 min, respectively. Cell viability was assessed using the LIVE/DEAD<sup>®</sup> Viability/Cytotoxicity Kit (Molecular Probes, Life Technologies) following the manufacturer's instructions. Briefly, the culture medium was poured out and the cells washed with PBS. The working solution containing 2 mM Calcein AM and 4 mM EthD-1 was then added directly to each well. After incubation at room temperature for 45 min, the cells were washed with PBS and then observed using a fluorescence microscope (emission at 515 nm and 635 nm) (Axio Observer, Zeiss, Germany) with a connected camera. Fluorescence images were collected using ZEN microscope software at five locations in each group.

## 2.9 Characterization

Transmission electron microscopy (TEM) and selected area electron diffraction (SAED) patterns were acquired using a JEOL JEM-2100F microscope operating at 200 kV. X-ray diffraction (XRD) analysis was conducted on a D8 Advance Bruker powder X-ray diffractometer with Cu K $\alpha$  radiation ( $\lambda = 1.5406 \text{ \AA}$ ) from  $10^\circ$  to  $80^\circ$  with a counting time of 1 s per step. To obtain the UC photoluminescence spectra, the NCs were dispersed in chloroform in a standard quartz cuvette at room temperature, and then were recorded by a Fluoromax-4, Horiba Jobin Yvon Spectrofluorometer. To obtain the emission spectra, sample excitation was accomplished using a diode laser, BWF-2 (980 nm,  $P_{\text{max}} = 2.0 \text{ W}$  at 3.0 A, B&W TEK Inc.) coupled to a 100  $\mu\text{m}$  (core) optical fiber. The emission spectra in the visible region were obtained with a resolution of 1 nm and a laser power of 1 W. UV-vis spectra were obtained using a CARY 5000 UV-Vis-NIR spectrophotometer. Gel permeation chromatography (GPC) was used to determine the molecular weight and polydispersity of the PMAO-PEG on a Waters e2695 Alliance system with Waters 2414 RI Detector. Downconversion fluorescence of Ce6, NC-Ce6 and supernatant was measured by using a Shimadzu RF-5301PC Spectrofluorometer fitted with a 150-W xenon lamp as the excitation source with a resolution of 1 nm. The FTIR measurement was conducted in a Digilab FTS 3100 instrument. Hydrodynamic size of NCs was measured via dynamic light scattering (DLS) in a Malvern Nano Zetasizer system by Malvern Instruments equipped with a HeNe 633 nm laser. Thermogravimetric analysis (TGA) was measured in a Perkin Elmer TGA/DTA instrument. The  $T_1$  and  $T_2$ -weighted images

were obtained on a 7 T Bruker ClinScan MRI system. All samples were dissolved in double distilled water. The repetition time (TR) and echo time (TE) were optimized for  $T_1$  or  $T_2$ . Other relevant acquisition parameters are: number of acquisitions = 16, field of view = 39 mm, slice thickness = 1 mm. All experiments were performed in 1% agarose medium. *In vivo* MR imaging were acquired using subcutaneous injection of the NC in a mouse model. Animal was anesthetized by inhalation of isoflurane. Body temperature was maintained at  $38 \pm 1^\circ\text{C}$ . The spin echo and gradient echo images were acquired with subcutaneous injection in the flank region of the mouse.

## 3. Results and Discussion

The transmission emission microscopy (TEM) images of the seed  $\text{NaDyF}_4\text{:Yb}^{3+}$  and  $\text{NaDyF}_4\text{:Yb}^{3+}/\text{NaGdF}_4\text{:Yb}^{3+}, \text{Er}^{3+}$  NCs are shown in Fig. 1b and 1c, respectively. The image of the seed NCs (Fig. 1b) displayed signs of anisotropic growth. The nanorods (NRs) in the presence of  $\text{Gd}^{3+}$  and  $\text{Er}^{3+}$  showed relatively uniform morphology, due to the well-defined orientation and growth. The average diameter and length of the  $\text{NaDyF}_4\text{:Yb}^{3+}$  are 17 and 22 nm ( $\pm 0.8$  nm), respectively. The average diameter and length of the  $\text{NaDyF}_4\text{:Yb}^{3+}/\text{NaGdF}_4\text{:Yb}^{3+}, \text{Er}^{3+}$  NRs are 21 and 45 nm ( $\pm 1$  nm), respectively. The hexagonal phase structure of the  $\text{NaDyF}_4\text{:Yb}^{3+}$  NCs and  $\text{NaDyF}_4\text{:Yb}^{3+}/\text{NaGdF}_4\text{:Yb}^{3+}, \text{Er}^{3+}$  NRs were confirmed by the XRD analysis (Fig. 1d). The peak positions and intensities of the seed NCs are consistent with hexagonal-phase  $\text{NaDyF}_4$ .<sup>27</sup> The XRD pattern of the  $\text{NaDyF}_4\text{:Yb}^{3+}/\text{NaGdF}_4\text{:Yb}^{3+}, \text{Er}^{3+}$  NRs is similar to that of the seed NCs, but with an increase in peak signal intensity. The increased intensity is attributed to the increase in size of the NCs and similar crystal structure of  $\text{NaDyF}_4$  and  $\text{NaGdF}_4$ . In addition, a smaller peak shift of (201) and (211) peaks, further suggest that  $\text{NaGdF}_4$  enriches the surface of the NRs.<sup>28</sup> Energy-dispersive X-ray analysis (EDX) confirmed the presence of all elements in the seed NCs (Na, Dy, F, Yb) and NRs (Gd, Er in addition to all seed elements) (Fig. S1A, S1B). Using inductively coupled plasma mass spectroscopy (ICP-MS), the Gd:Dy molar ratio was quantified to be 40.2:40 which was in agreement with the stoichiometric ratio of the chloride precursors.

In order to demonstrate the feasibility of our strategy, five types of NCs were synthesized: (i)  $\text{NaGdF}_4\text{:Yb}^{3+}, \text{Er}^{3+}$ ; (ii)  $\text{NaDyF}_4\text{:Yb}^{3+}/\text{NaGdF}_4\text{:Yb}^{3+}, \text{Er}^{3+}$ ; (iii)  $\text{Yb}^{3+}$ -absent  $\text{NaDyF}_4/\text{NaGdF}_4\text{:Yb}^{3+}, \text{Er}^{3+}$ ; (iv) triple-doped  $\text{NaGdF}_4\text{:Yb}^{3+}, \text{Er}^{3+}, \text{Dy}^{3+}$  and (v)  $\text{NaDyF}_4\text{:Yb}^{3+}, \text{Er}^{3+}/\text{NaGdF}_4$ . Fig. 2a shows the UC emission spectra of the different NCs excited at 980 nm. All the NCs exhibited green and red emissions. There are no characteristic emissions of  $\text{Dy}^{3+}$  in the wavelength regions of 470-500 nm and 570-600 nm, indicating that  $\text{Yb}^{3+}$  act as the main sensitizer and only  $\text{Er}^{3+}$  as the emitters. Therefore, green emissions at 523 and 546 nm are ascribed to  $\text{Er}^{3+}$  transitions of  $^2\text{H}_{11/2} \rightarrow ^4\text{I}_{15/2}$  and  $^4\text{S}_{3/2} \rightarrow ^4\text{I}_{15/2}$ , respectively, while red emission at 659 nm is due to the  $\text{Er}^{3+}$  transition of  $^4\text{F}_{9/2} \rightarrow ^4\text{I}_{15/2}$ .<sup>29, 30</sup> The intensities of green emissions of all NCs are much stronger in comparison with those of red emission, therefore, all NCs show green colour (Fig. 2bii-2bvi). The current emission properties of the NCs present a proof-of-concept, of which their emissions can be further tuned when doped with other lanthanide ions such as



Tm<sup>3+</sup> or Ho<sup>3+</sup> to give single colour emission across the visible and NIR spectrum for specific biomedical applications.<sup>31, 32</sup>

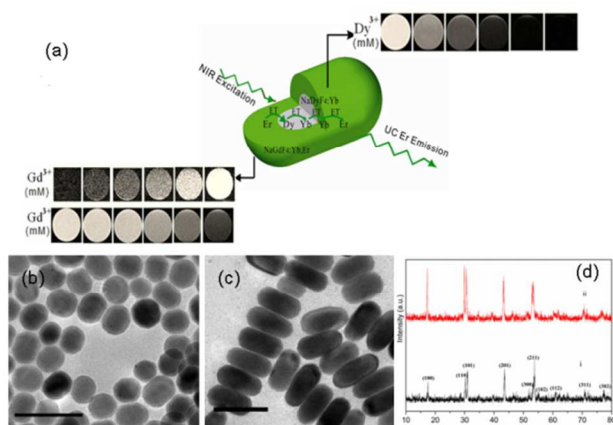


**Fig.1** (a) Schematic illustration of the general strategy to achieve tunable MRI T<sub>1</sub>-T<sub>2</sub> contrast and UC lanthanide NCs; TEM images of (b) NaDyF<sub>4</sub>:Yb<sup>3+</sup> and (c) NaDyF<sub>4</sub>:Yb<sup>3+</sup>/NaGdF<sub>4</sub>:Yb<sup>3+</sup>,Er<sup>3+</sup> NCs; (d) XRD patterns of as-synthesized (i) NaDyF<sub>4</sub>:Yb<sup>3+</sup> and (ii) NaDyF<sub>4</sub>:Yb<sup>3+</sup>/NaGdF<sub>4</sub>:Yb<sup>3+</sup>,Er<sup>3+</sup> NCs (scale bar: 50 nm).

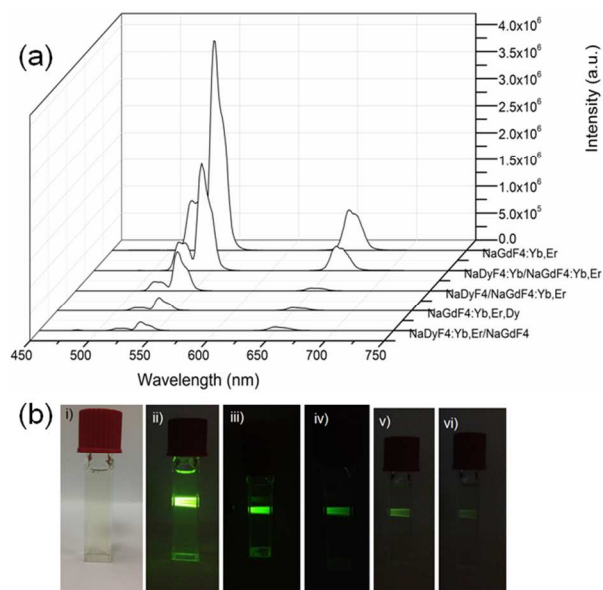


**Fig.2** (a) UC fluorescence spectra of NaGdF<sub>4</sub>:Yb<sup>3+</sup>,Er<sup>3+</sup>; NaDyF<sub>4</sub>:Yb<sup>3+</sup>/NaGdF<sub>4</sub>:Yb<sup>3+</sup>,Er<sup>3+</sup>; Yb<sup>3+</sup>-absent NaDyF<sub>4</sub>/NaGdF<sub>4</sub>:Yb<sup>3+</sup>,Er<sup>3+</sup>; triple dopant NaGdF<sub>4</sub>:Yb<sup>3+</sup>,Er<sup>3+</sup>,Dy<sup>3+</sup> and NaDyF<sub>4</sub>:Yb<sup>3+</sup>,Er<sup>3+</sup>/NaGdF<sub>4</sub> NCs at the excitation of 980 nm. (b) Photographs of (i) NaDyF<sub>4</sub>:Yb<sup>3+</sup>/NaGdF<sub>4</sub>:Yb<sup>3+</sup>,Er<sup>3+</sup> under nature light; UC green emissions of (ii) NaGdF<sub>4</sub>:Yb<sup>3+</sup>,Er<sup>3+</sup>; (iii) NaDyF<sub>4</sub>:Yb<sup>3+</sup>/NaGdF<sub>4</sub>:Yb<sup>3+</sup>,Er<sup>3+</sup>; (iv) Yb<sup>3+</sup>-absent NaDyF<sub>4</sub>/NaGdF<sub>4</sub>:Yb<sup>3+</sup>,Er<sup>3+</sup>; (v) triple doped NaGdF<sub>4</sub>:Yb<sup>3+</sup>,Er<sup>3+</sup>,Dy<sup>3+</sup> and (vi) NaDyF<sub>4</sub>:Yb<sup>3+</sup>,Er<sup>3+</sup>/NaGdF<sub>4</sub> NC. All samples were dispersed in chloroform (1 mg/ml), spectra were recorded at a power of 1 W.

The intensities of the green emissions of NCs (ii)-(v) are weaker than that of (i) NaGdF<sub>4</sub>:Yb<sup>3+</sup>,Er<sup>3+</sup>, due to the quenching effect of Dy<sup>3+</sup>. One explanation for Dy<sup>3+</sup> quenching of Er<sup>3+</sup> luminescence is the depopulation of <sup>4</sup>I<sub>11/2</sub> (Er<sup>3+</sup>) and <sup>2</sup>F<sub>5/2</sub> (Yb<sup>3+</sup>) by Dy<sup>3+</sup>. Since the <sup>2</sup>F<sub>5/2</sub>→<sup>2</sup>F<sub>7/2</sub> transition of Yb<sup>3+</sup> ions and <sup>4</sup>I<sub>11/2</sub>→<sup>4</sup>I<sub>15/2</sub> transition of Er<sup>3+</sup> ions are resonant with the <sup>6</sup>H<sub>5/2</sub>→<sup>6</sup>H<sub>15/2</sub> transition of Dy<sup>3+</sup>, energy transfer between Yb<sup>3+</sup>, Er<sup>3+</sup> and Dy<sup>3+</sup> can readily take place (Fig. 3). Dy<sup>3+</sup> can receive energy from the excited Yb<sup>3+</sup> and Er<sup>3+</sup>, or excited by 980 nm photon, populating

the <sup>6</sup>H<sub>5/2</sub> excited state from <sup>6</sup>H<sub>15/2</sub> ground state. The life time of <sup>6</sup>H<sub>5/2</sub> is short, and so back-energy transfer to Yb<sup>3+</sup> is negligible.<sup>33</sup> The excited Dy<sup>3+</sup> can either relax radiatively to ground state or relax non-radiatively to the <sup>6</sup>H<sub>9/2</sub> level, of which the transition energy is transferred to the Er<sup>3+</sup> for excitation from the ground level (<sup>4</sup>I<sub>15/2</sub>) to the first excitation level (<sup>4</sup>I<sub>13/2</sub>). The second and third energy transfers from the Dy<sup>3+</sup> to Er<sup>3+</sup> at the <sup>4</sup>I<sub>13/2</sub> can cause Er<sup>3+</sup> excitation from the first excitation level (<sup>4</sup>I<sub>13/2</sub>) to a higher <sup>4</sup>F<sub>9/2</sub> level and subsequently to the upper excitation level (<sup>2</sup>H<sub>9/2</sub>). A radiative transition from <sup>2</sup>H<sub>9/2</sub> to <sup>4</sup>I<sub>11/2</sub> level ensues and gives rise to red emission around 660 nm. This three-photon excitation process has been demonstrated by a study of UC Er<sup>3+</sup> emissions in the presence of Dy<sup>3+</sup>.<sup>33</sup> However, the efficiency of this three-photon excitation is low compared to the Yb<sup>3+</sup>-Er<sup>3+</sup> energy transition process. As sensitizers, Yb<sup>3+</sup> has only one excitation level at 980 nm and exhibits a much larger absorption cross-section at this level, working more efficiently as sensitizing centre in comparison with Dy<sup>3+</sup>.

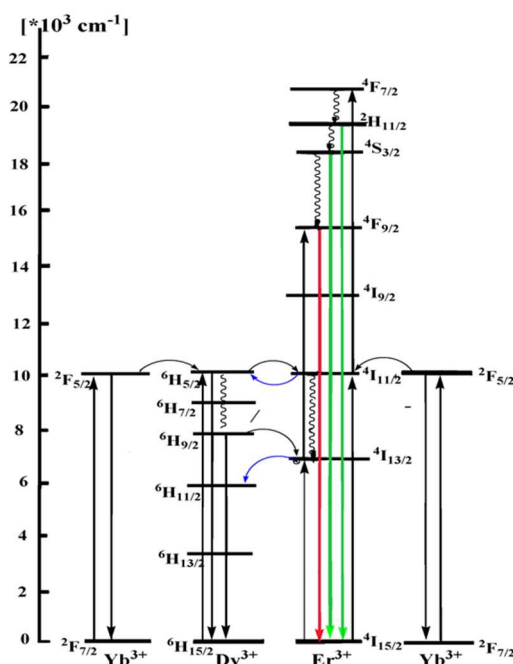


**Fig.3** Proposed energy transfer processes responsible for the UC emission of NaGdF<sub>4</sub>:Yb<sup>3+</sup>,Er<sup>3+</sup>; NaDyF<sub>4</sub>:Yb<sup>3+</sup>/NaGdF<sub>4</sub>:Yb<sup>3+</sup>,Er<sup>3+</sup>; Yb<sup>3+</sup>-absent NaDyF<sub>4</sub>/NaGdF<sub>4</sub>:Yb<sup>3+</sup>,Er<sup>3+</sup>; triple dopant NaGdF<sub>4</sub>:Yb<sup>3+</sup>,Er<sup>3+</sup>,Dy<sup>3+</sup> and NaDyF<sub>4</sub>:Yb<sup>3+</sup>,Er<sup>3+</sup>/NaGdF<sub>4</sub> NCs. Vertical and wavy arrows represent non-radiative transitions, curved arrows represent non-radiative energy transfer, green and red arrows represent green and red emissions.

NaDyF<sub>4</sub>:Yb<sup>3+</sup>/NaGdF<sub>4</sub>:Yb<sup>3+</sup>,Er<sup>3+</sup> (ii) and NaDyF<sub>4</sub>/NaGdF<sub>4</sub>:Yb<sup>3+</sup>,Er<sup>3+</sup> (iii) NCs show stronger emission than triple doped NaGdF<sub>4</sub>:Yb<sup>3+</sup>,Er<sup>3+</sup>,Dy<sup>3+</sup> (iv) and NaDyF<sub>4</sub>:Yb<sup>3+</sup>,Er<sup>3+</sup>/NaGdF<sub>4</sub> (v) (Fig. 2a), highlighting the advantages of the current NCs with varying composition to circumvent the detrimental effect of Dy<sup>3+</sup>. The emitters Er<sup>3+</sup> ions are physically separated from the Dy<sup>3+</sup>, minimizing the energy transfers to Dy<sup>3+</sup> which led to quenching of Er<sup>3+</sup> luminescence. By comparing the NaDyF<sub>4</sub>:Yb<sup>3+</sup>/NaGdF<sub>4</sub>:Yb<sup>3+</sup>,Er<sup>3+</sup> (ii) and NaDyF<sub>4</sub>/NaGdF<sub>4</sub>:Yb<sup>3+</sup>,Er<sup>3+</sup> (iii), it was observed that the UC emission intensity was further enhanced upon doping the core with Yb<sup>3+</sup> (in the case of (ii)). Dopant concentration determines

the distance between two neighbouring ions and has a great impact on the efficiency of energy transfer and hence the UC efficiency of lanthanide ions doped NCs.<sup>9</sup> Increasing Yb<sup>3+</sup> population in the core “tricks” the Dy<sup>3+</sup> to undergo energy transfer with the “sacrificial” Yb<sup>3+</sup> ions, reduces the quenching effect on the Er<sup>3+</sup>. The increase in Yb<sup>3+</sup> sensitization centres also facilitates greater population of Er<sup>3+</sup> to the <sup>4</sup>F<sub>7/2</sub> state via two successive energy transfers (<sup>4</sup>I<sub>15/2</sub> → <sup>4</sup>I<sub>11/2</sub>, <sup>4</sup>I<sub>11/2</sub> → <sup>4</sup>F<sub>7/2</sub>), of which Er<sup>3+</sup> ions decay to give rise to green (<sup>2</sup>H<sub>11/2</sub> → <sup>4</sup>I<sub>15/2</sub>, <sup>4</sup>S<sub>3/2</sub> → <sup>4</sup>I<sub>15/2</sub>) and red (<sup>4</sup>F<sub>9/2</sub> → <sup>4</sup>I<sub>15/2</sub>) emissions (Fig. 3, Fig. S2). It should be noted that the presence of Gd<sup>3+</sup> should not affect the above-discussed energy transfer due to the large energy gap (32,000 cm<sup>-1</sup>) between the ground <sup>8</sup>S<sub>7/2</sub> and first excited states <sup>6</sup>P<sub>7/2</sub>.

The NaDyF<sub>4</sub>:Yb<sup>3+</sup>/NaGdF<sub>4</sub>:Yb<sup>3+</sup>,Er<sup>3+</sup> NCs (referred as NCs hereafter) were rendered water-dispersible using PEG polymer and the fluorescence intensity of the NCs was slight decreased (Fig. S3-S8).<sup>26</sup> The hydrodynamic sizes of NCs before and after PMAO-PEG functionalization were determined to be 56 nm and 84 nm, respectively by DLS (Fig S5). The size increase (~28 nm) is attributed to the PEG coating and the water molecules associated to PEG. We evaluated the colloidal stability of PEG functionalized NCs in water, and no significant size change was observed up to 7 days, demonstrating the excellent colloidal stability of the PMAO-PEG functionalized NCs (Fig. S6).

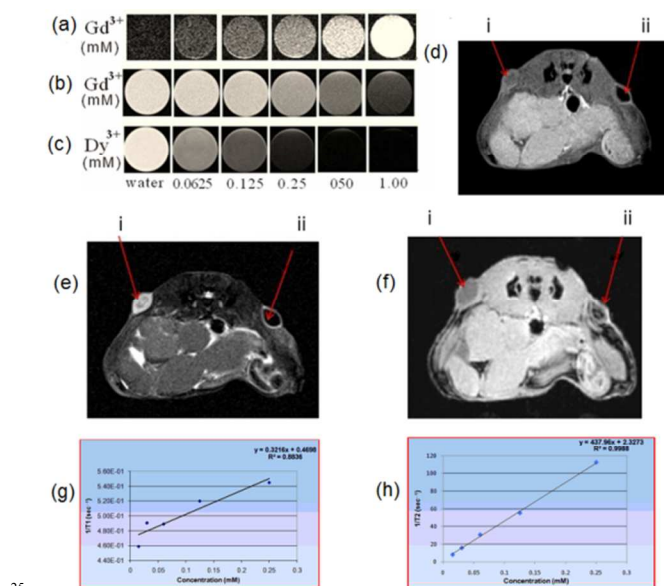


**Fig.4** (a) Bright T<sub>1</sub>-weighted phantom MR images using gradient echo sequence. (b) Dark T<sub>1</sub>-weighted phantom images using spin echo sequence; (c) T<sub>2</sub>-weighted phantom images of NaDyF<sub>4</sub>:Yb<sup>3+</sup>/NaGdF<sub>4</sub>:Yb<sup>3+</sup>,Er<sup>3+</sup> NCs at different concentrations (0, 0.0625, 0.125, 0.50, 1.00 mM). (d) T<sub>1</sub>-weighted MR image using spin echo sequence; (e) T<sub>2</sub>-weighted image using spin echo sequence and (f) T<sub>1</sub>-weighted image using gradient echo sequence with an inversion pulse of NaDyF<sub>4</sub>:Yb<sup>3+</sup>/NaGdF<sub>4</sub>:Yb<sup>3+</sup>,Er<sup>3+</sup> NCs fixed in 0.8% agarose, injected subcutaneously in mouse model. (i) represents control, 0.8% agarose. (ii) represents NC fixed in 0.8% agarose; (g) and (h) T<sub>2</sub> relaxation time plot of NaDyF<sub>4</sub>:Yb<sup>3+</sup>/NaGdF<sub>4</sub>:Yb<sup>3+</sup>,Er<sup>3+</sup> NCs. Spin echo sequence were used to measure the T<sub>1</sub> and T<sub>2</sub> relaxation time constant. The experimental parameters for T<sub>1</sub>- and T<sub>2</sub>-weighted images are TR/TE/NEX = 400/8.9/16 and TR/TE/NEX = 1500/41/16, respectively.

**40** *In vitro* T<sub>1</sub>- and T<sub>2</sub>-weighted MR images of the NCs were measured as a function of metal concentration using a 7 T MRI

system (Fig. 4a-4c). As expected, the NCs show excellent negative T<sub>2</sub> enhancement in the spin echo (SE) based T<sub>2</sub>-weighted MR phantom (Fig. 4c). Interestingly, tunable positive and negative T<sub>1</sub> enhancement from the NCs can also be achieved by suitably employing a magnetization preparation module in a gradient echo (GE) or a SE sequence. In Fig. 4a, the images were acquired with a GE T<sub>1</sub>-weighted sequence with a magnetization preparation (inversion pulse) module, which exhibits a positive T<sub>1</sub> contrast, while Fig. 4b shows T<sub>1</sub>-weighted images acquired with a SE sequence without any preparation module, which clearly shows negative enhancement albeit the parameters were optimized.

The r<sub>1</sub> and r<sub>2</sub> relaxivities of the NCs have been determined as 0.321 and 437.97 mM<sup>-1</sup>s<sup>-1</sup>, respectively (Fig. 4g, 4h). The r<sub>2</sub> is higher than other reported Dy<sub>2</sub>-based materials in the literature to the best of our knowledge.<sup>12, 35-40</sup> Generally, for T<sub>1</sub> and T<sub>2</sub> materials in direct contact, the magnetic field generated by T<sub>2</sub> materials perturbs the relaxation process of the paramagnetic T<sub>1</sub> contrast element. We believe that the enhancement of T<sub>2</sub> relaxivity of the NCs compared to the NaDyF<sub>4</sub> NPs could be due to the additional synergistic contribution of T<sub>2</sub> shortening by the Gd<sup>3+</sup> sitting adjacent to Dy<sup>3+</sup> in the NRs. Moreover, because of the high susceptibility of the Gd<sup>3+</sup>, the slight increase of local magnetic field probably led to the significant synergistic impact on relaxation rates and resulted in very high T<sub>2</sub> relaxation.<sup>41</sup>

Gd<sup>3+</sup> ions are known to show excellent bright T<sub>1</sub> enhancing properties.<sup>42-44</sup> As discussed, the current NRs generate T<sub>1</sub> negative contrast in the normal SE based T<sub>1</sub>-weighted experiments (in the absence of an inversion module). Any T<sub>1</sub> CAs, including Gd<sup>3+</sup>-based CAs, demonstrate both T<sub>1</sub> and T<sub>2</sub> relaxation properties, but generally shortening of T<sub>1</sub> is dominated over that of T<sub>2</sub> which result in a hyperintense image within areas where the agents are taken up.<sup>42</sup> Thus, species with high T<sub>1</sub> values lend themselves to hypointense images.<sup>42</sup> The r<sub>1</sub> of NCs obtained from SE (0.321 mM<sup>-1</sup>s<sup>-1</sup>), is much smaller than that of other T<sub>1</sub> of Gd<sup>3+</sup>-based materials, for example Gadovist (commercially Gd-based CAs, r<sub>1</sub> = 4.34 mM<sup>-1</sup>s<sup>-1</sup>),<sup>42</sup> Gd<sub>2</sub>O<sub>3</sub> nanoparticles (8.8 mM<sup>-1</sup>s<sup>-1</sup> for size 2.2 nm and 4.4 mM<sup>-1</sup>s<sup>-1</sup> for size 4.6 nm),<sup>45</sup> ultrasmall Gd<sub>2</sub>O<sub>3</sub> NRs (1.5 mM<sup>-1</sup>s<sup>-1</sup>),<sup>46</sup> and GdF<sub>3</sub> (3.17 mM<sup>-1</sup>s<sup>-1</sup>),<sup>47</sup> indicating the T<sub>1</sub> relaxation of water is large in these NCs and hence capable of inducing negative contrast. The presence of Dy<sup>3+</sup> is inferred to affect the T<sub>1</sub> induced by the Gd<sup>3+</sup> ions (due to the very short electronic relaxation time of Dy<sup>3+</sup> compared to Gd<sup>3+</sup> ions), hence leading to the current observation of negative T<sub>1</sub> contrast. Cheon and co-workers reported similar findings, that the coupling process between the electron spins of the T<sub>1</sub> CA and nuclear spins of water is perturbed in the presence of additional magnetic field generated by T<sub>2</sub> CA in close proximity.<sup>14</sup> One of the strategies to increase the relaxivity is to enhance the exchange rate of water between the NPs and the water in the bulk phase.<sup>14</sup> The water exchange rate of Dy<sup>3+</sup> is generally faster than that of the Gd<sup>3+</sup>. Therefore, the measured low r<sub>1</sub> could be attributed to the slow water exchange rate of Gd<sup>3+</sup> which is presented in the outer layer of our NCs. In addition, the relaxivity measurements at high field (7 T) (as Gd<sup>3+</sup> relaxivity drops significantly at high fields<sup>48, 49</sup>) and the relatively larger size of NCs in the current work (i.e. less surface Gd<sup>3+</sup> ions to volume ratio) are two possible reasons that might account for the lower r<sub>1</sub> (per mM basis) of the current NCs.

The results are in agreement with the study by Cheon's group, where smaller size and higher surface area NCs, showed a higher MR relaxivity attributed to better magnetic exchange with surrounding water protons.<sup>50</sup>

Despite a weak  $T_1$  negative contrast, a  $T_1$  positive contrast was also obtained in a GE sequence when an inversion module was used at the start of the pulse sequence. The GE is generated by fast gradient reversal which allows minimum echo time and repetition time, and is characterized by rapid sampling time. Since the signal is detected rapidly during the recovery of the longitudinal magnetization, this sequence generates a good  $T_1$  positive contrast.

To examine the feasibility of the NCs for *in vivo* application, we performed subcutaneous injection of the NCs in a mouse model. It is apparent from the images that the NCs generate a negative  $T_1$  and  $T_2$  contrast for a SE sequence, in addition to positive  $T_1$  contrast when using a GE with a preparation module consisting of an inversion pulse, with an inversion delay of 1800 ms (Fig. 4d-4f). Thus, the NCs are capable of generating tunable  $T_1$  and  $T_2$  contrast by choosing appropriate MRI sequences. In addition to possessing the advantages of normal positive  $T_1$  CAs for clear visualization of anatomic details and bright contrast for distinguishing from other pathogenic or biological condition, the current NCs also possess the advantages of negative  $T_1$  CAs. Generally the  $T_2$ -weighted experiment consumes more experimental time, because of large TR and TE, than the  $T_1$ -weighted experiments. Since our NCs generate negative  $T_1$  enhancement (small TR and TE), they could find application in cases where negative contrast is desired within a limited experimental time. Therefore, depending on the tissue site of interest, the current NCs can be selectively tuned to visualize by bright or dark  $T_1$ - and  $T_2$ -weighted MRI contrast in order to obtain complementary information. In addition, the image quality can also be improved, leading to more accurate diagnosis. The relaxivities of the current NCs may be optimized by varying the concentration of the dopants and/or introducing a physical barrier between the  $Dy^{3+}$  and  $Gd^{3+}$ , so as to reduce the effect of  $Dy^{3+}$  on  $Gd^{3+}$ . It is noteworthy that the size of the as-synthesized NCs is not optimal as bioimaging probes, which can be tuned to sub-10 nm size by varying reaction conditions of the current synthesis method.<sup>51, 52</sup> Sub-10 nm NCs can be cleared from the body more efficiently, enabling the possibility of using higher dosage of imaging probes.<sup>53, 54</sup> The main objective of this work is to demonstrate a proof-of-concept of the current lanthanide-based nanostructure as a bioimaging agent, and future works may include optimization of NCs size and functionality.

To demonstrate the feasibility of using NCs in PDT, PS Ce6 was conjugated to the NCs, as the red emission from the NCs matched well with the absorption peak of Ce6. The NCs-Ce6 complex formed greenish clear solution with good stability in water (Fig. 5a). To confirm Ce6 was indeed loaded on NCs instead of being encapsulated by the PEG polymer, solutions of free Ce6, NCs-Ce6, and PEG polymer mixed with Ce6 were prepared and centrifuged at 10,000 rpm for 10 min. While neither precipitate nor color change was noted for free Ce6 and PEG + Ce6 samples after centrifugation, a dark green solid and nearly colorless supernatant were observed after the mixture of NC + Ce6 was centrifuged, indicating the binding of Ce6 on NCs which

were pulled down by the centrifugation force (Fig. S9). After centrifugation, the supernatant was saved. The fluorescence spectra of free Ce6, NCs-Ce6 and the supernatant were measured under 400 nm excitation (Fig. S10). The fluorescence of Ce6 was notably quenched once it was loaded on NCs, suggesting the intermolecular interactions between Ce6 and NCs surface. The supernatant showed no fluorescence, indicating that there was no leakage of the Ce6 from the NCs. The loading efficiency of NCs-Ce6 complex studies showed that the Ce6 loading capacity increased with the increasing Ce6 concentration and saturated at 6-7% at Ce6 concentration above 1 mM (Fig. S11, S12). To evidence the energy transfer between NCs and the loaded Ce6, we measured the UC emission spectra of NCs-Ce6 complexes at different Ce6 concentration using 980 nm excitation (Fig. 5a). While bare NCs gave three strong emission peaks at 523 nm (green), 546 nm (green) and 660 nm (red), the conjugation of Ce6 on NCs resulted in a significant quenching of the red peak with increasing Ce6 loading, due to the resonance energy transfer from the NCs to the nearby Ce6 molecules, which had an absorption peak right at 660 nm. Green emissions only affected slightly after the Ce6 loading.

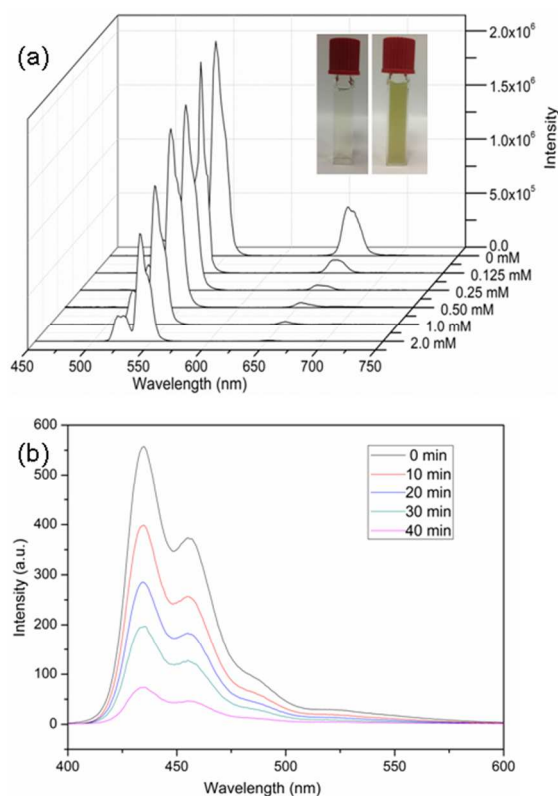


**Fig.5** (a) UC emission spectra of NCs-Ce6 complex at different Ce6 concentration under 980 excitation. Concentration of the NCs in samples was kept the same. Insert: photographs of NCs (colorless) and NCs-Ce6 solutions (greenish). (b) Change of DMA fluorescence due to the generation of singlet oxygen from NCs-Ce6 under 980 nm irradiation.

Generation of ROS is crucial in PDT and it was measured using DMA as a rapid chemical trap for singlet oxygen. DMA is a fluorescent compound ( $\lambda_{\text{excitation}} = 375$  nm,  $\lambda_{\text{emission}} = 436$  nm) that reacts selectively with  $^1O_2$  to form the non-fluorescent 9,10-endoperoxide with a relatively high quenching rate constant and unique selectivity for singlet oxygen. Fig. 5b shows the



fluorescence for a DMA solution after NCs-Ce6 was irradiated using a 980 nm laser ( $1 \text{ W/cm}^2$ ) for different period of time. The amount of singlet oxygen produced by NCs-Ce6 could then be determined by the fluorescence quenching of DMA. The fluorescence intensity gradually decreases with the increase of irradiation time, confirming the generation of singlet oxygen by energy transfer from NCs to Ce6. Control experiments involving NCs and Ce6 were carried out for comparison and it is obvious that fluorescence quenching effect from DMA reaction can not be observed for the NCs and Ce6 (Fig. S13).

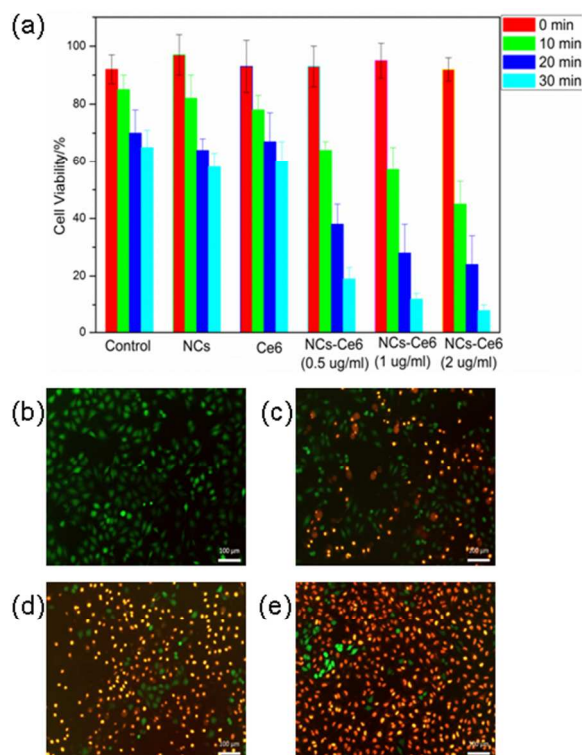


**Fig.6** (a) Cell viability of HeLa cells with/without treatment of pure NCs, Ce6 and NCs-Ce6 at different concentration of NCs-Ce6 at radiation time of 0 min, 10 min, 20 min, 30 min, respectively. Detection of photodamage by fluorescence microscopy using fluorescent probes at the NCs-Ce6 concentration of  $0.5 \mu\text{g/ml}$  at time of (b) 0 min, (c) 10 min, (d) 20 min, (e) 30 min, respectively (double-staining with calcein-AM and ethidium homodimer).

*In vitro* cytotoxicity evaluation of the NCs with and without Ce6 in HeLa cells using alamar blue<sup>®</sup> assays showed that these NCs had a cell viability of greater than 90% up to  $16 \mu\text{g/ml}$  for 24 h and a relatively low toxicity investigated for 72 h at  $37^\circ\text{C}$ , indicating their suitability for biomedical application (Fig. S14). The PDT effect was investigated *in vitro* by measuring HeLa cell viability incubated with free Ce6, bare NCs and NCs-Ce6 for 1 h, and irradiated with a NIR laser for 0 min, 10 min, 20 min and 30 min, respectively. A significantly decrease in cell viability with NCs-Ce6 was shown after 980 nm laser irradiation (up to 30 min,  $1 \text{ W/cm}^2$ ) (Fig. 6a). The cell death rate showed dose-dependent and time-dependent manner. As shown in control experiments, cell death was observed due to the overheating problem associated with 980 nm laser irradiation; however, cells viability was still up to 75% with the treatment of 1 min irradiation time

interval to release the heat from the cell medium. no obvious reduction in cell viabilities was noticed for cells incubated with free Ce6 or bare NCs in the presence of NIR light irradiation after subtracting the cell death due to the laser heating problem (Fig. 6a), indicating that free Ce6 and bare NCs with irradiation did not produce cancer cells-killing singlet oxygen. In order to further investigate the PDT efficiency of NCs-Ce6, cell viability was also determined by staining live and dead cells with calcein-AM and ethidium homodimer, respectively. Live and dead cells were visualized as green and red light emission. After 10 min of irradiation on the NCs-Ce6 treated cells (concentration from  $0.5 \mu\text{g/ml}$  to  $2 \mu\text{g/ml}$ ), cell death initiated and significantly reduced cell viability were observed after 30 min NIR irradiation (Fig. 6b-e and Fig. S15). Cell viability decreased with increasing concentration of NCs-Ce6. These results have clearly demonstrated the feasibility of NCs-Ce6 as PDT agents.

#### 4. Conclusions

The current work has demonstrated a simple strategy to fabricate NCs possessing tunable negative and positive  $T_1$  and  $T_2$  MR contrasts with efficient UC fluorescence, which is solely based on active lanthanide elements. The key strategy involves physically separating the  $T_2$  “poisoning”  $\text{Dy}^{3+}$  ions from the  $\text{Er}^{3+}$  emitters, and by co-doping  $\text{Dy}^{3+}$  with  $\text{Yb}^{3+}$  activators. In addition to the ability to show strong  $T_2$  contrast, by utilizing a different pulse sequence, positive and negative  $T_1$  contrasts can be tuned. The successful circumventing of the UC poisoning effect of  $\text{Dy}^{3+}$  ions enables the demonstration of near-infrared activated UC PDT in cancer cells ablation. The study suggests that the current NCs may be feasible as a new generation of “smart” theranostic probes in the area of image-guided diagnosis and therapy.

#### Acknowledgments

The authors acknowledge Singapore Ministry of Education AcRF Tier 2 ARC16/11 and BMRC A\*STAR for funding support.

#### References

1. T. D. Schladt, K. Schneider, M. I. Shukoor, F. Natalio, H. Bauer, M. N. Tahir, S. Weber, L. M. Schreiber, H. C. Schroder, W. E. G. Muller and W. Tremel, *J. Mater. Chem.*, 2010, **20**, 8297.
2. F. Wang, X. Chen, Z. Zhao, S. Tang, X. Huang, C. Lin, C. Cai and N. Zheng, *J. Mater. Chem.*, 2011, **21**, 11244.
3. X. Song, H. Gong, S. Yin, L. Cheng, C. Wang, Z. Li, Y. Li, X. Wang, G. Liu and Z. Liu, *Adv. Funct. Mater.*, 2013, **24**, 1194.
4. Q. Tian, J. Hu, Y. Zhu, R. Zou, Z. Chen, S. Yang, R. Li, Q. Su, Y. Han and X. Liu, *J. Am. Chem. Soc.*, 2013, **135**, 8571.
5. Y. Ma, X. Liang, S. Tong, G. Bao, Q. Ren and Z. Dai, *Adv. Funct. Mater.*, 2013, **23**, 815.
6. H. Chen, S. Li, B. Li, X. Ren, D. M. Mahounga, S. Cui, Y. Gu and S. Achilefu, *Nanoscale*, 2012, **4**, 6050.
7. I. Miladi, C. Alric, S. Dufort, P. Mowat, A. Dutour, C. Mandon, G. Laurent, E. Bräuer-Krisch, N. Herath, J. L. Coll, M. Dutreix, F. Lux, R. Bazzi, C. Billotey, M. Janier, P. Perriat, G. Le Duc, S. Roux and O. Tillement, *Small*, 2014, **10**, 1116.
8. H. Benachour, A. Sève, T. Bastogne, C. Frochot, R. Vanderesse, J. D. Jasnowski, I. Miladi, C. Billotey, O. Tillement, F. Lux and M. Barberi-Heyob, *Theranostics*, 2012, **2**, 889.



9. F. Wang and X. Liu, *Chem. Soc. Rev.*, 2009, **38**, 976.
10. D. K. Chatterjee, L. S. Fong and Y. Zhang, *Adv. Drug Delivery Rev.*, 2008, **60**, 1627.
11. F. Auzel, *Chem. Rev.*, 2004, **104**, 139.
12. G. K. Das, N. J. J. Johnson, J. Cramen, B. Blasiak, P. Latta, B. Tomanek and F. C. J. M. van Veggel, *J. Phys. Chem. Lett.*, 2012, **3**, 524.
13. M. Norek, E. Kampert, U. Zeitler and J. A. Peters, *J. Am. Chem. Soc.*, 2008, **130**, 5335.
14. J. S. Choi, J. H. Lee, T. H. Shin, H. T. Song, E. Y. Kim and J. Cheon, *J. Am. Chem. Soc.*, 2010, **132**, 11015.
15. K. H. Bae, Y. B. Kim, Y. Lee, J. Y. Hwang, H. Park and T. G. Park, *Bioconjugate Chem.*, 2010, **21**, 505.
16. H. Yang, Y. Zhuang, Y. Sun, A. Dai, X. Shi, D. Wu, F. Li, H. Hu and S. Yang, *Biomaterials*, 2011, **32**, 4584.
17. T. Courant, V. G. Roullin, C. Cadiou, M. Callewaert, M. C. Andry, C. Portefaix, C. Hoeffel, M. C. De Goltstein, M. Port, S. Laurent, L. V. Elst, R. Muller, M. Molinari and F. Chuburu, *Angew. Chem. Int. Ed.*, 2012, **51**, 9119.
18. H. Chen, B. Qi, T. Moore, D. C. Colvin, T. Crawford, J. C. Gore, F. Alexis, O. T. Mefford and J. N. Anker, *Small*, 2014, **10**, 160.
19. G. H. Im, S. M. Kim, D. G. Lee, W. J. Lee, J. H. Lee and I. S. Lee, *Biomaterials*, 2013, **34**, 2069.
20. F. Hu, Q. Jia, Y. Li and M. Gao, *Nanotechnology*, 2011, **22**, 245604.
21. J.-C. Boyer, J. Gagnon, L. A. Cuccia and J. A. Capobianco, *Chem. Mater.*, 2007, **19**, 3358.
22. Z. Li, Zhang, Y., Jiang, S., *Adv. Mater.*, 2008, **20**, 4765.
23. H. Ralph A, *J. Lumin.*, 1970, **1-2**, 778.
24. F. V. J. C. Boyer, J. A. Capobianco, A. Speghini, M. Bettinelli, *Chem. Phys. Lett.*, 2004, **390**, 403.
25. J. Park, K. An, Y. Hwang, J. E. G. Park, H. J. Noh, J. Y. Kim, J. H. Park, N. M. Hwang and T. Hyeon, *Nat. Mater.*, 2004, **3**, 891.
26. W. W. Yu, E. Chang, J. C. Falkner, J. Zhang, A. M. Al-Somali, C. M. Sayes, J. Johns, R. Drezek and V. L. Colvin, *J. Am. Chem. Soc.*, 2007, **129**, 2871.
27. H.-X. Mai, Y.-W. Zhang, R. Si, Z.-G. Yan, L.-D. Sun, L.-P. You and C.-H. Yan, *J. Am. Chem. Soc.*, 2006, **128**, 6426.
28. K. A. Abel, J.-C. Boyer and F. C. J. M. van Veggel, *J. Am. Chem. Soc.*, 2009, **131**, 14644.
29. J. C. Boyer, L. A. Cuccia and J. A. Capobianco, *Nano Lett.*, 2007, **7**, 847.
30. J. C. Boyer, F. Vetrone, L. A. Cuccia and J. A. Capobianco, *J. Am. Chem. Soc.*, 2006, **128**, 7444.
31. Y. Zhang, J. D. Lin, V. Vijayaragavan, K. K. Bhakoo and T. T. Y. Tan, *Chem. Commun.*, 2012, **48**, 10322.
32. Q. C. Xu, Y. Zhang, M. J. Tan, Y. Liu, S. Yuan, C. Choong, N. S. Tan and T. T. Y. Tan, *Adv. Healthcare Mater.*, 2012, **1**, 470.
33. Y. F. Yasuo S., *Jpn. J. Appl. Phys.*, 1971, **10**, 891.
34. V. Mahalingam, R. Naccache, F. Vetrone and J. A. Capobianco, *Chem. Commun.*, 2011, **47**, 3481.
35. L. Vander Elst, A. Roch, P. Gillis, S. Laurent, F. Botteman, J. W. M. Bulte and R. N. Muller, *Magnet. Reson. Med.*, 2002, **47**, 1121.
36. G. K. Das, Y. Zhang, L. D'Silva, P. Padmanabhan, B. C. Heng, J. S. C. Loo, S. T. Selvan, K. K. Bhakoo and T. T. Y. Tan, *Chem. Mater.*, 2011, **23**, 2439.
37. K. Kattel, J. Y. Park, W. Xu, H. G. Kim, E. J. Lee, B. A. Bony, W. C. Heo, S. Jin, J. S. Baeck, Y. Chang, T. J. Kim, J. E. Bae, K. S. Chae and G. H. Lee, *Biomaterials*, 2012, **33**, 3254.
38. J. Zhou, Z. Lu, G. Shan, S. Wang and Y. Liao, *Biomaterials*, 2014, **35**, 368.
39. Y. Zhang, V. Vijayaragavan, G. K. Das, K. K. Bhakoo and T. T. Y. Tan, *Eur. J. Inorg. Chem.*, 2012, 2044.
40. R. J. Holmberg, T. Aharen and M. Murugesu, *J. Phys. Chem. Lett.*, 2012, **3**, 3721.
41. Z. Zhou, D. Huang, J. Bao, Q. Chen, G. Liu, Z. Chen, X. Chen and J. Gao, *Adv. Mater.*, 2012, **24**, 6223.
42. M. Bottrill, L. Kwok and N. J. Long, *Chem. Soc. Rev.*, 2006, **35**, 557.
43. P. Caravan, *Chem. Soc. Rev.*, 2006, **35**, 512.
44. P. Caravan, J. J. Ellison, T. J. McMurry, R. B. Lauffer, *Chem. Rev.*, 1999, **99**, 2293.
45. J.-L. Bridot, A.-C. Faure, S. Laurent, C. Rivière, C. Billotey, B. Hiba, M. Janier, V. Jossereand, J.-L. Coll, L. Vander Elst, R. Muller, S. Roux, P. Perriat and O. Tillement, *J. Am. Chem. Soc.*, 2007, **129**, 5076.
46. G. K. Das, B. C. Heng, S.-C. Ng, T. White, J. S. C. Loo, L. D'Silva, P. Padmanabhan, K. K. Bhakoo, S. T. Selvan and T. T. Y. Tan, *Langmuir*, 2010, **26**, 8959.
47. F. Evanics, P. R. Diamante, F. C. J. M. van Veggel, G. J. Stanisz, R. S. Prosser, *Chem. Mater.*, 2006, **18**, 2499.
48. L. Helm, *Future Med. Chem.*, 2010, **2**, 385.
49. Y. Gossuin, A. Hocq, Q. L. Vuong, S. Disch, R. P. Hermann and P. Gillis, *Nanotechnology*, 2008, **19**, 475102.
50. Y.-W. Jun, J.-H. Lee and J. Cheon, *Angew. Chem. Int. Ed.*, 2008, **47**, 5122.
51. S. Y. Kim, K. Woo, K. Lim, K. Lee and H. S. Jang, *Nanoscale*, 2013, **5**, 9255.
52. G. K. Das, B. C. Heng, S. C. Ng, T. White, J. S. C. Loo, L. D'Silva, P. Padmanabhan, K. K. Bhakoo, S. T. Selvan and T. T. Y. Tan, *Langmuir*, 2010, **26**, 8959.
53. G. Chen, T. Y. Ohulchanskyy, R. Kumar, H. Ågren and P. N. Prasad, *ACS Nano*, 2010, **4**, 3163.
54. M. Longmire, P. L. Choyke and H. Kobayashi, *Nanomedicine*, 2008, **3**, 703.